JACS
JOURNAL OF THE AMERICAN CHEMICAL SOCIETY

Article

pubs.acs.org/JACS

Chemical Manipulation of Magnetic Ordering in $Mn_{1-x}Sn_xBi_2Se_4$ Solid−Solutions

Kulugammana G. S. Ranmohotti, Honore Djieutedjeu, and Pierre F. P. Poudeu*

Laboratory for Emerging Energy and Electronic Materials, Department of Materials Science and Engineering, University of Michigan, Ann Arbor, Michigan 48109, United States

Supporting Information

ABSTRACT: Several compositions of manganese−tin−bismuth selenide solid−solution series, $Mn_{1-x}Sn_xBi_2Se_4$ (x = 0, 0.3, 0.75), were synthesized by combining high purity elements in the desired ratio at moderate temperatures. X-ray single crystal studies of a Mn-rich composition (x = 0) and a Mn-poor phase (x = 0.75) at 100 and 300 K revealed that the compounds crystallize isostructurally in the monoclinic space group $C2/m$ (no.12) and adopt the $MnSb_2Se_4$ structure type. Direct current (DC) magnetic susceptibility measurements in the temperature range from 2 to 300 K indicated that the dominant magnetic ordering within the $Mn_{1-x}Sn_xBi_2Se_4$ solid−solutions below 50 K switches from antiferromagnetic (AFM) for $MnBi_2Se_4$ (x = 0), to ferromagnetic (FM) for $Mn_{0.7}Sn_{0.3}Bi_2Se_4$ (x = 0.3), and finally to paramagnetic (PM) for $Mn_{0.25}Sn_{0.75}Bi_2Se_4$ (x = 0.75). We show that this striking variation in the nature of magnetic ordering within the $Mn_{1-x}Sn_xBi_2Se_4$ solid−solution series can be rationalized by taking into account: (1) changes in the distribution of magnetic centers within the structure arising from the Mn to Sn substitutions, (2) the contributions of spin-polarized free charge carriers resulting from the intermixing of Mn and Sn within the same crystallographic site, and (3) a possible long-range ordering of Mn and Sn atoms within individual $\{M\}_nSe_{4n+2}$ single chain leading to quasi isolated $\{MnSe_6\}$ octahedra spaced by nonmagnetic $\{SnSe_6\}$ octahedra.

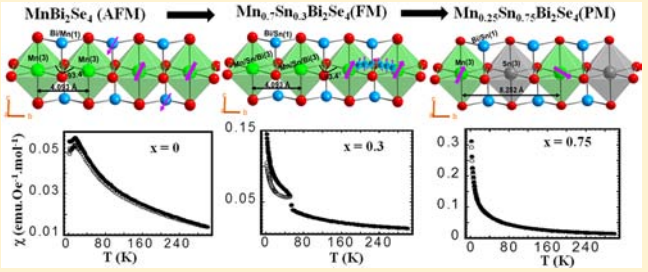

INTRODUCTION

There is a fast growing interest in exploiting the low crystal symmetry as well as the structural diversity and flexibility associated with multinary metal chalcogenides to design novel multifunctional materials and to chemically manipulate interactions between coexisting functionalities.[1−11] The renewed interest in this family of compounds has been motivated by a continuing discovery of a large number of synthetic and natural metal chalcogenides exhibiting a tremendous variety of physical properties.[12−17] In addition, multinary metal chalcogenides are generally used in next-generation technologies such as thermoelectrics,[18,19] nonlinear optics,[20,21] photoelectronics,[22] and solid-state electrolytes.[23,24] One fascinating feature of multinary heavy main-group metal chalcogenides is their ability to form homologous series of closely related structures.[12,14,17,25−30] The size, shape and chemical composition of various structural subunits building the three-dimensional structure of these homologous series of structures can generally be manipulated independently making the engineering of the physical properties of local crystal atomic sublattices possible. The application of this concept resulted in the formation of regularly spaced subdomains with distinct functionalities within a single crystal structure.[1,3,4] For example, we recently demonstrated that the crystal chemistry of $Pb_4Sb_4Se_{10}$,[31] the selenium analogue of the mineral cosalite, can be manipulated to create ordered magnetic subdomains, with increasing structural and chemical complexity, periodically dispersed within the three-dimensional framework of Pb, Sb and Se. This resulted in several $Fe_xPb_{4-x}Sb_4Se_{10}$ compositions featuring the coexistence of ferromagnetism and semiconductivity above room temperature.[1] Another fascinating family of compounds under investigation is the ternary MPn_2Se_4 (M = Fe, Mn; Pn = Sb, Bi) phases.[3,4] These compounds crystallize isostructurally in the monoclinic space group $C2/m$ and adopt crystal structure similar to that of the order member N = 3 of the pavonite homologous series defined with the general composition $M'_{N+1}Bi_2S_{N+5}$ (M′ = Ag, Sn, Pb, Bi).[32] The magnetic and electronic properties of MPn_2Se_4 (M = Fe, Mn; Pn = Sb, Bi) phases strongly depend on the nature of the M and Pn atoms. For instance, we have observed from magnetic and electronic transport measurements that the Fe containing MSb_2Se_4 compound is a p-type single-chain ferromagnetic semiconductor,[3] while the Mn phase is a p-type semiconducting single-chain antiferromagnet.[4]

In this work, we investigate the crystal structure of the manganese bismuth analogue $Mn_{1-x}Sn_xBi_2Se_4$, and explore the interplay between the local atomic structural ordering arising from Sn substitution at Mn positions and the magnetic exchange coupling within individual single magnetic chains and between neighboring single chains in the three-dimensional structure.

Received: April 24, 2012
Published: August 1, 2012

   dx.doi.org/10.1021/ja303952w | J. Am. Chem. Soc. 2012, 134, 14033−14042

Initial investigation of the crystal structure of $MnBi_2Se_4$ by Lee et al. using single crystals grown in an alkali halide flux reported a defect structure with compositions $Mn_{1-x}Bi_{2+y}Se_4$ ($0.1 \leq x \leq 0.14$; $y = 0.667x$) in which, ~20% vacancy was found at the Mn($2d$) site while Bi/Mn mixed occupancy at a 60/40 ratio was adopted for the Mn($2a$) position.[33] Another structural model derived using neutron diffraction data from polycrystalline samples, with full (100%) Mn($2d$) site occupancy, 70%Bi + 30%Mn mixed occupancy at Mn($2a$) site and 93%Bi + 7%Mn mixed occupancy at both Bi positions, was later proposed by Kurowski.[34] Our investigation of the crystal structure of $MnBi_2Se_4$ using X-ray single crystal data at 100 and 300 K confirms the latter structural model as the more accurate description of the distribution of Mn and Bi atoms within the structure. We observed that gradual Mn to Sn substitution in the $Mn_{1-x}Sn_xBi_2Se_4$ solid solution series drastically changes the distribution of Mn atoms among various metal positions within the structure leading to the formation of either isolated one-dimensional $\{M\}_nSe_{4n+2}$ single magnetic chains or isolated $\{M\}Se_6$ zero-dimensional magnetic centers (M = Mn/Sn, Mn/Bi, or Mn/Bi/Sn) linked by nonmagnetic {(Bi/Sn)Se} semiconducting ribbons. The magnetic behavior of selected $Mn_{1-x}Sn_xBi_2Se_4$ compositions is rationalized within the context of the distribution of magnetic centers within the crystal structure.

EXPERIMENTAL SECTION

Synthesis. Polycrystalline powders of $Mn_{1-x}Sn_xBi_2Se_4$ (x = 0, 0.3, and 0.75) were synthesized using high purity Mn metal powder (CERAC, 99.8%), Sn powder (CERAC, 99.99%), Bi metal pieces (Aldrich, 99.999%), and Se powder (CERAC, 99.999%) as starting materials. The constituting elements, weighed in the desired ratio (total mass = 10 g) under argon atmosphere in a dry glovebox, were well mixed in an agate mortar with pestle and transferred into a fused silica tube ($\varnothing_{ID}$ = 7 mm, length =18−24 cm). The tube was flame-sealed under residual pressure of $\sim 10^{-3}$ Torr. The sealed tubes were then inserted into mullite tubes and isolated using ceramic fibers. This precaution is necessary to minimize the temperature gradient inside the quartz tube during the reaction. The protected-tubes were then placed into tube furnaces and heat treated following two different temperature profiles.

In the case of $MnBi_2Se_4$, the furnace temperature was raised to 973 K in 12 h, dwelled for 96 h followed by cooling to room temperature in 12 h. The resulting product was a dark gray polycrystalline single-phase powder of $MnBi_2Se_4$. Single crystals of $MnBi_2Se_4$ suitable for X-ray structure determination were grown by annealing the as prepared polycrystalline single phase powder at 1000 K for seven days followed by cooling to room temperature in 24 h.

For $Mn_{1-x}Sn_xBi_2Se_4$ compositions with x = 0.3 and 0.75, the furnace temperature was initially raised to 573 K in 4 h and dwelled for 24 h to allow low melting elements such as Sn, Bi and Se to react. The furnace temperature was finally raised to 823 K, dwelled for 72 h and slowly cooled to 473 K over 48 h followed by fast cooling to room temperature. A second dwelling cycle at 723 K for 72 h was necessary to complete the reaction and improve the crystallinity of the samples. The resulting products for both reactions were dark gray polycrystalline powders. Single crystals with composition $Mn_{0.25}Sn_{0.75}Bi_2Se_4$ suitable for X-ray structure determination were obtained from the polycrystalline powders after the second dwelling cycle.

Characterization. *X-ray Powder Diffraction.* The phase purity of the synthesized $Mn_{1-x}Sn_xBi_2Se_4$ (x = 0, 0.3 and 0.75) polycrystalline samples were assessed by recording X-ray diffraction patterns on finely ground powders using Cu−K_α radiation (λ = 1.54056 Å) in reflection geometry on a PANalytical X-ray powder diffractometer with position sensitive detector and operating at 45 kV and 40 mA. The experimental X-ray diffraction patterns of the synthesized materials (Figure 1A) were compared to the theoretical pattern of $MnBi_2Se_4$ simulated using single crystal structure data.

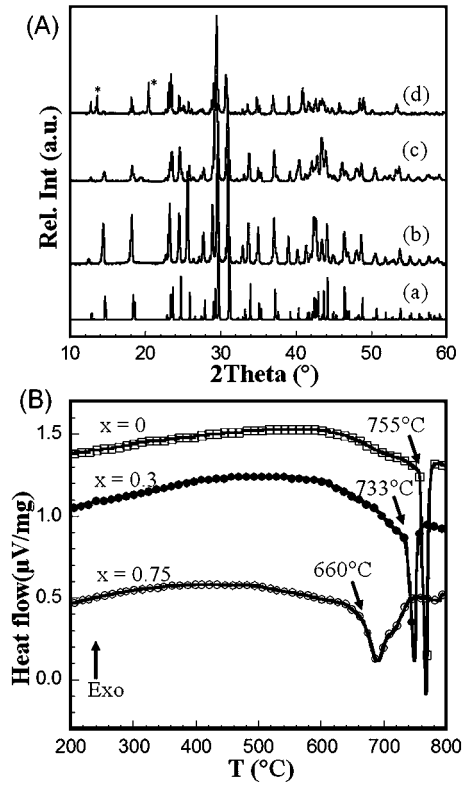

Figure 1. (A) Experimental X-ray diffraction patterns of $Mn_{1-x}Sn_xBi_2Se_4$ compared with the theoretical pattern (a) calculated from the single crystal structure refinement of $MnBi_2Se_4$; (b) x = 0; (c): x = 0.3; and (d) x = 0.75; (*) correspond to additional peaks of the $Sn_{0.571}Bi_{2.286}Se_4$ (~10%) impurity phase. (B) Differential scanning calorimetry (DSC) curves of $Mn_{1-x}Sn_xBi_2Se_4$ (x = 0, 0.3, and 0.75) showing endothermic peaks corresponding to melting upon heating.

Differential Scanning Calorimetry (DSC). To further confirm the phase purity of the synthesized $Mn_{1-x}Sn_xBi_2Se_4$ (x = 0, 0.3, and 0.75) materials and also to determine their melting temperatures, DSC measurements were performed on finely ground powders. DSC data were recorded using approximately 10 mg of the synthesized materials and an equivalent mass of alumina (Al_2O_3) as the reference. Both the sample and the reference, sealed in a small quartz tube under residual pressure of 10^{-3} Torr, were placed on the sample and reference pans of a F401 DSC apparatus (NETZSCH) maintained under flowing nitrogen gas. The sample and reference were simultaneously heated to 1073 K at a rate of 20 K/min, isothermed for 2 min and then cooled to 473 K at a rate of 20 K/min. DSC data were recorded during two heating and cooling cycles. The endothermic onset temperatures are reported as the melting points (Figure 1B).

Single Crystal Structure Determination. Single crystals of $MnBi_2Se_4$ (0.05 × 0.06 × 0.15 mm^3) and $Mn_{0.25}Sn_{0.75}Bi_2Se_4$ (0.03 × 0.06 × 0.1 mm^3) were mounted on the tip of a glass fiber using a two-component epoxy glue and intensity data were recorded at 100 and 300 K ($MnBi_2Se_4$) and at 300 K ($Mn_{0.25}Sn_{0.75}Bi_2Se_4$) on a STOE IPDS-2T diffractometer using a graphite-monochromated Mo K_α radiation (λ = 0.71073 Å). The intensity data were best indexed in the monoclinic crystal system with unit cell parameters: a = 13.319(3)/*13.384(3)* Å; b = 4.0703(8)/*4.0925(8)* Å, c = 15.179(3)/*15.224(3)* Å, β = 115.5(1)/*115.6(1)*° for $MnBi_2Se_4$ at 100 K/*300 K;* and a = 13.4932(6) Å; b = 4.1260(2) Å, c = 15.3224(7) Å, β = 115.5(1)° for $Mn_{0.25}Sn_{0.75}Bi_2Se_4$ at 300 K.

$MnBi_2Se_4$. The structure of $MnBi_2Se_4$ at 300 K was refined with the SHELTXL[35] package of programs in the space group $C2/m$ (no.12)

dx.doi.org/10.1021/ja303952w | J. Am. Chem. Soc. 2012, 134, 14033−14042

using the atomic coordinates of $MnSb_2Se_4$ as the starting model.[4] In the first refinement cycle, Bi atoms were assigned to M1(4*i*) and M2(4*i*) positions located, respectively, in a distorted octahedral and square pyramidal environment, while Mn atoms were located in the M3(2*d*) and M4(2*a*) octahedral sites. Although the refinement of this model using a full-matrix least-squares method resulted in reasonable isotropic atomic displacement parameters for most atoms, the thermal parameter for Mn4 was disproportionally small compared to those of the other atoms. This suggested a Mn/Bi mixed occupancy at M4 position. The refinement of this model resulted in more uniform thermal parameters for all atoms, but the final composition showed an excess of positive charges. In order to get a charge balanced composition, Bi/Mn mixed occupancy was also introduced to the M1 and M2 positions and an electroneutrality restraint was applied. The refinement of this model using a secondary extinction correction and anisotropic displacement parameters for all atoms resulted in the final atomic distribution M1 = 94% Bi + 6% Mn, M2 = 94% Bi + 6% Mn, M3 = 100% Mn, and M4 = 24% Bi + 76% Mn, corresponding to the final charge balanced composition $Mn_{1.00(3)}Bi_{2.00(3)}Se_4$, assuming 2+, 3+, and 2− oxidation states for Mn, Bi, and Se, respectively. The observed distribution of Mn and Bi atoms at various metal positions and the assigned oxidation state of Mn and Bi atoms are consistent with the results of bond valence sum (BVS) calculations,[36] (M1(Bi), 3.1; M2(Bi), 3.3; M2(Mn), 2.0; M4(Mn/Bi), 1.7). A similar distribution of Mn and Bi at the M1, M2, M3 and M4 positions was obtained from the structure refinement using intensity data collected at 100 K.

$Mn_{0.25}Sn_{0.75}Bi_2Se_4$. A strategy similar to the one described above was used for the refinement of the structure of $Mn_{0.25}Sn_{0.75}Bi_2Se_4$. The observed unit cell parameters of a = 13.4932(6) Å; b = 4.1260(2) Å, c = 15.3224(7) Å, β = 115.5(1)° are very close to those of the ternary $MnBi_2Se_4$ phase, suggesting a similarity in their crystal structures. Therefore, the atomic positions of $MnBi_2Se_4$ were used in the first refinement cycle with all metal positions (M1 to M4) initially assigned to Bi. The refinement of this model resulted in the agreement factor R_1 ∼ 15% with very high isotropic atomic displacement parameter for Bi4, which was about 10 times that of Bi2. The thermal parameters of Bi1and Bi3 were about twice that of Bi2. We then assumed that Bi1(M1), Bi3(M3) and Bi4(M4) positions were partially occupied by lighter atoms. In the subsequent model, mixed occupancy between Bi and Sn was assumed at the M1, M3 and M4 positions. The refinement yielded R_1 ∼ 8% with reasonable thermal parameters for the M1 and M4 positions. The M3 atom still showed an isotropic thermal parameter about 4 times that of Bi2, M1 and M4. We therefore assumed the M3 position to be occupied by an element lighter than Bi. In the next model, bismuth was removed from the M3 position and a mixed occupancy between Sn and Mn was assumed. The refinement yielded a more acceptable displacement parameter for the M3 position. In subsequent refinement cycles, a secondary extinction correction as well as anisotropic displacement parameters for all atoms was included. The composition of the crystal was freely refined to the final atomic distribution: M1 = 80% Bi + 20% Sn, M2 = 100% Bi, M3 = 50% Mn + 50% Sn, and M4 = 40% Bi + 60% Sn resulting in the chemical composition $Mn_{0.25(2)}Sn_{0.75(2)}Bi_{2.00(2)}Se_4$.

Summary of crystallographic data for $MnBi_2Se_4$ and $Mn_{0.25}Sn_{0.75}Bi_2Se_4$ is given in Table 1. The atomic coordinates and isotropic displacement parameters of all atoms for both $MnBi_2Se_4$ (at 100 and 300 K) and $Mn_{0.25}Sn_{0.75}Bi_2S_4$ (at 300 K) structures are given in Table 2. Selected interatomic distances are gathered in Table 3. The software Diamond[37] was utilized to create the graphic representation of the crystal structures with ellipsoid representations (98% probability level) for all atoms. Further details of the crystal structure investigation are given in CIF format as Supporting Information.

X-ray Photoelectron Spectroscopy (XPS). To probe the chemical composition as well as determining the oxidation state of Mn, Sn and Bi in the synthesized $Mn_{1-x}Sn_xBi_2Se_4$ (x = 0, 0.3, and 0.75) materials, XPS spectra of all samples were recorded, under the same condition, on a Kratos Axis Ultra XPS using a monochromated aluminum anode.

Magnetic Susceptibility Measurements. The direct current (DC) magnetic susceptibilities of $Mn_{1-x}Sn_xBi_2Se_4$ (x = 0, 0.3, and 0.75) materials were investigated from 2 to 300 K using a Quantum Design MPMS-XL SQUID magnetometer. Approximately 50 mg of the as synthesized polycrystalline $Mn_{1-x}Sn_xBi_2Se_4$ (x = 0, 0.3, and 0.75) powder materials was mounted inside a clear plastic straw sample holder, the magnetic moment contribution of which was subtracted from the combined (sample + sample holder) measurement. DC magnetic susceptibility data were collected using applied magnetic fields of 100 and 10 000 Oe. A field-dependent magnetization measurement was performed at 2 K on the composition with x = 0.3 using up to 50 kOe applied magnetic field.

Table 1. Selected Crystallographic Data for $Mn_{1-x}Sn_xBi_2Se_4$ (x = 0, 0.75)

formula sum	$MnBi_2Se_4$ (100 K/*300 K*)	$Mn_{0.25}Sn_{0.75}Bi_2Se_4$ (300 K)
Crystal system; space group	Monoclinic; *C*2/*m* (#12)	
Formula weight (g/mol)	788.74	836.55
Density Calc. (g/cm^3)	7.05/*6.96*	7.22
Lattice parameters (Å)		
a =	13.319(3)/ *13.384(3)*	13.493(6)
b =	4.0703(8)/ *4.0925(8)*	4.126(2)
c =	15.179(3)/ *15.224(3)*	15.322(7)
β (°) =	115.5(1)/ *115.6(1)*	115.5(1)
Volume (Å^3); Z	742.8(4)/ *752.4(4)*; 4	769.8(4); 4
Radiation (Å)	λ (Mo K_α) = 0.71073	
μ (cm^{-1})	684/*676*	672
Diff. elec. density [eÅ^{-3}]	+3.13 to −2.24/ + 2.70 to −2.02	+ 3.62 to −2.71
R_1 ($F_o > 4\sigma(F_o)$)[a]	0.039/*0.025*	0.049
wR_2 (all)[b]	0.073/*0.06*	0.10
GoF	1.104/*1.115*	1.356

[a] $R_1 = \sum||F_o| - |F_c||/\sum|F_o|$; [b] $wR_2 = [\sum w(F_o^2 - F_c^2)^2/\sum w(F_o^2)^2]^{1/2}$

RESULTS AND DISCUSSION

Synthesis and Characterization. The formation of high crystallinity single-phase product of the $Mn_{1-x}Sn_xBi_2Se_4$ ($0 \le x \le 1$) solid-solutions is challenging. We found from several unsuccessful synthetic attempts using various strategies, that the formation of high purity $Mn_{1-x}Sn_xBi_2Se_4$ samples is difficult to achieve using slow or fast cooling from the melts. This is mainly due to the poor thermal stability of the compounds above the melting temperature and the high tendency to crystallize thermodynamically stable binary phases such as Bi_2Se_3 and SnSe during cooling. The most successful strategy in the formation of single-phase products consists of reacting the constituent elements at temperatures lower than the melting point of the targeted composition. Using powder X-ray diffraction (XRD) and differential scanning calorimetry (DSC) (Figure 1), we have established that for the formation of $Mn_{1-x}Sn_xBi_2Se_4$ single phase product, the temperature of the furnace should be maintained between 723 and 823 K for at least three days. Multiple ramping and dwelling steps from room temperature are necessary to prevent the evaporation of Se during the heating cycle. Because of the low temperature of the reaction, the crystallinity of the final product is generally poor and postreaction annealing at 773 K for up to seven days is often necessary to bring the reaction product into thermodynamic equilibrium. The comparison of the experimental X-ray powder diffraction pattern of $MnBi_2Se_4$ with the theoretical pattern calculated from the single crystal structure refinement of $MnBi_2Se_4$ (Figure 1A) showed excellent agreement. This indicates successful formation of $MnBi_2Se_4$ single phase and also validates the accuracy of the proposed

dx.doi.org/10.1021/ja303952w | J. Am. Chem. Soc. 2012, 134, 14033−14042

Table 2. Wyckoff Positions (W.P.), Site Occupancy Factors (k), Atomic Coordinates and Equivalent Isotropic Displacement Parameters ($U_{eq}/10^{-4} \times Å^2$) for All Atoms in the Asymmetric Unit of $Mn_{1-x}Sn_xBi_2Se_4$ (x = 0, 0.75)[a]

site	atom	W.P.	k	x	y	z	U_{eq}[b]
M1	Bi1|Mn1	4*i*	0.94|0.06	0.2816(2)	0	0.6371(2)	106(2)
	Bi1|Mn1	4*i*	0.94|0.06	0.2814(2)	0	0.6373(2)	209(3)
	Bi1|Sn1	4*i*	0.80|0.20	0.2823(2)	0	0.6384(2)	235(5)
M2	Bi2|Mn2	4*i*	0.94|0.06	0.3510(2)	0	0.1303(2)	105(2)
	Bi2|Mn2	4*i*	0.94|0.06	0.3509(2)	0	0.1305(2)	178(3)
	Bi2	4*i*	1	0.3516(2)	0	0.1329(1)	218(5)
M3	Mn3	2*d*	1	0	1/2	1/2	154(2)
	Mn3	2*d*	1	0	1/2	1/2	268(3)
	Mn3|Sn3	2*d*	0.50|0.50	0	1/2	1/2	312(6)
M4	Bi4|Mn4	2*a*	0.24|0.76	0	0	0	87(2)
	Bi4|Mn4	2*a*	0.24|0.76	0	0	0	168(3)
	Bi4|Sn4	2*a*	0.40|0.60	0	0	0	233(6)
Se1	Se1	4i	1	0.0115(2)	0	0.1851(2)	135(3)
	Se1	4i	1	0.0111(2)	0	0.1849(2)	209(3)
	Se1	4i	1	0.0098(3)	0	0.1901(3)	208(8)
Se2	Se2	4i	1	0.1138(2)	0	0.4549(2)	82(1)
	Se2	4i	1	0.1140(2)	0	0.4547(2)	151(3)
	Se2	4i	1	0.1155(3)	0	0.4563(2)	152(7)
Se3	Se3	4i	1	0.6584(2)	0	0.0607(2)	102(3)
	Se3	4i	1	0.6587(2)	0	0.0610(2)	170(3)
	Se3	4i	1	0.6630(3)	0	0.0633(2)	182(7)
Se4	Se4	4i	1	0.3417(2)	0	0.3250(2)	110(3)
	Se4	4i	1	0.3415(2)	0	0.3251(2)	183(3)
	Se4	4i	1	0.3385(3)	0	0.3230(2)	160(7)

[a]For each atomic site, the first, second, and third lines refer to $MnBi_2Se_4$ at 100 and 300 K, and $Mn_{0.25}Sn_{0.75}Bi_2Se_4$ at 300 K, respectively. [b]U_{eq} is defined as one-third of the trace of the orthogonalized U_{ij} tensor

Table 3. Selected Interatomic Distances (Å) in $Mn_{1-x}Sn_xBi_2Se_4$ (x = 0, 0.75)[a]

bond type	$MnBi_2Se_4$ 100 K	$MnBi_2Se_4$ 300 K	$Mn_{0.25}Sn_{0.75}Bi_2Se_4$ 300 K
M1−Se2	2.706(2)	2.717(2)	2.727(4)
M1−Se4$^{i, ii}$	2.824(2)	2.835(2)	2.844(3)
M1−Se2$^{i, ii}$	3.115(2)	3.130(2)	3.161(3)
M1−Se1$^{i, ii}$	3.552(2)	3.569(2)	3.561(3)
M2−Se1$^{iii, iv}$	2.806(2)	2.818(2)	2.823(3)
M2−Se3^{v}	2.847(2)	2.862(2)	2.927(4)
M2−Se4	3.012(2)	3.019(2)	2.993(4)
M2−Se3$^{vi, vii}$	3.082(2)	3.094(2)	3.087(3)
M3−Se4$^{ii, vii}$	2.584(2)	2.592(2)	2.648(3)
M3−Se2,2 $^{xi, xii, xiii}$	2.794(1)	2.810(2)	2.834(2)
M4−Se1, 1^{viii}	2.747(2)	2.755(2)	2.858(4)
M4−Se3 $^{vi, vii, ix, x}$	2.787(2)	2.804(2)	2.863(3)

[a]Operators for generating equivalent atoms: (i) $^1/_2 - x, -^1/_2 - y, 1 - z$; (ii) $^1/_2 - x, ^1/_2 - y, 1 - z$; (iii) $^1/_2 + x, ^1/_2 + y, z$; (iv) $^1/_2 + x, -^1/_2 + y, z$; (v) $1 - x, -y, -z$; (vi) $-^1/_2 + x, -^1/_2 + y, z$; (vii) $-^1/_2 + x, ^1/_2 + y, z$; (viii) $-x, -y, -z$; (ix) $^1/_2 - x, -^1/_2 - y, -z$; (x) $^1/_2 - x, ^1/_2 - y, -z$; (xi) $-x, -y, 1 - z$; (xii) $x, 1 + y, z$; (xiii) $-x, 1 - y, 1 - z$.

structural model. X-ray powder patterns of the $Mn_{1-x}Sn_xBi_2Se_4$ (x = 0.3 and 0.75) solid-solutions also showed good match with the theoretical pattern of $MnBi_2Se_4$ single phase (except for the Sn-rich (x = 0.75), which showed additional peaks corresponding to $Sn_{0.571}Bi_{2.286}Se_4$[38] as a minor (~10%) impurity phase) indicating similarity in their crystal structures. The observed high level of isomorphic substitution between Mn and Sn (up to 75%) within the $Mn_{1-x}Sn_xBi_2Se_4$ solid-solution series is quite surprising and largely deviates from the Goldschmidt's substitution rules,[39] giving the large difference between the effective ionic radii of Mn and Sn in octahedral coordination.[40,41] The presence of $Sn_{0.571}Bi_{2.286}Se_4$ as impurity phase only in the Sn-rich sample $Mn_{0.25}Sn_{0.75}Bi_2Se_4$ (x = 0.75) suggests that this composition borders the upper limit of the $Mn_{1-x}Sn_xBi_2Se_4$ solid-solution series. DSC analysis showed that the synthesized $Mn_{1-x}Sn_xBi_2Se_4$ compositions melt congruently between 660 and 760 °C and the melting temperature gradually decreases with increasing Sn content (Figure 1B). This trend is consistent with the gradual substitution of high melting Mn atoms by low melting Sn atoms in the structure of $MnBi_2Se_4$.

Careful examination of XPS spectra (Figure 2) revealed the presence of all elements in various $Mn_{1-x}Sn_xBi_2Se_4$ samples. The observed decrease in the intensity of Mn $2p_{3/2}$ peak (Figure 2A) and the increase in the Sn 3d peaks (Figure 2B) in various $Mn_{1-x}Sn_xBi_2Se_4$ samples are consistent with gradual substitution of Mn by Sn in the $Mn_{1-x}Sn_xBi_2Se_4$ nominal starting compositions. The XPS spectra of Mn $2p_{3/2}$ in various $Mn_{1-x}Sn_xBi_2Se_4$ samples is shown in Figure 2A and the observed binding energy peaks ranging from ~640 eV to ~641 eV are comparable to the binding energy (~640.2 eV) reported for Mn^{2+} $2p_{3/2}$ in MnSe.[42] This suggests that Mn atoms in the synthesized $Mn_{1-x}Sn_xBi_2Se_4$ samples exist in a 2+ valence state. Figure 2B displays XPS spectra for the Sn 3d doublet ($3d_{5/2}$ and $3d_{3/2}$ at 486.2 and 494.4 eV, respectively) recorded for the $Mn_{1-x}Sn_xBi_2Se_4$ samples. These values of the Sn $3d_{5/2}$ and Sn $3d_{3/2}$ binding energy are similar to those reported for Sn 3d peaks in SnSe ($3d_{5/2}$: 486.1 eV and $3d_{3/2}$: 494.8 eV).[43] In addition, the similarity of the binding energy difference of the Sn 3d doublet in $Mn_{1-x}Sn_xBi_2Se_4$ samples (8.2 eV), SnSe (8.7 eV)[43] and SnS (8.4 eV)[44] strongly indicates that the chemical state of Sn atoms in $Mn_{1-x}Sn_xBi_2Se_4$ samples is indeed 2+. No additional peaks at higher energies that can be assigned to Sn^{4+}

dx.doi.org/10.1021/ja303952w | J. Am. Chem. Soc. 2012, 134, 14033−14042

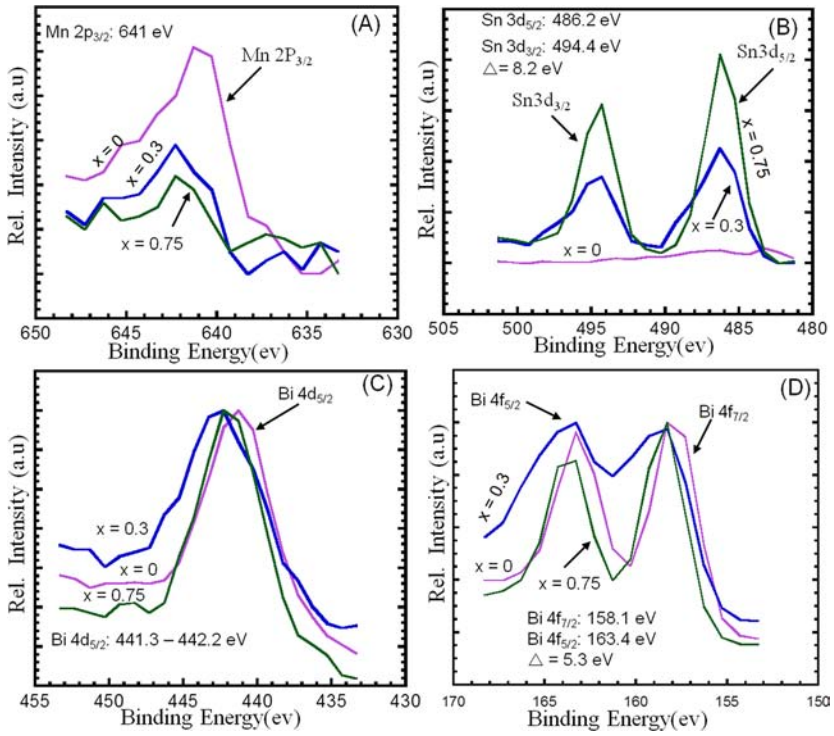

Figure 2. Comparison of XPS spectra of $Mn_{1-x}Sn_xBi_2Se_4$ samples: Mn 2p (A), Sn 3d (B), Bi 4d (C), and Bi 4f (D).

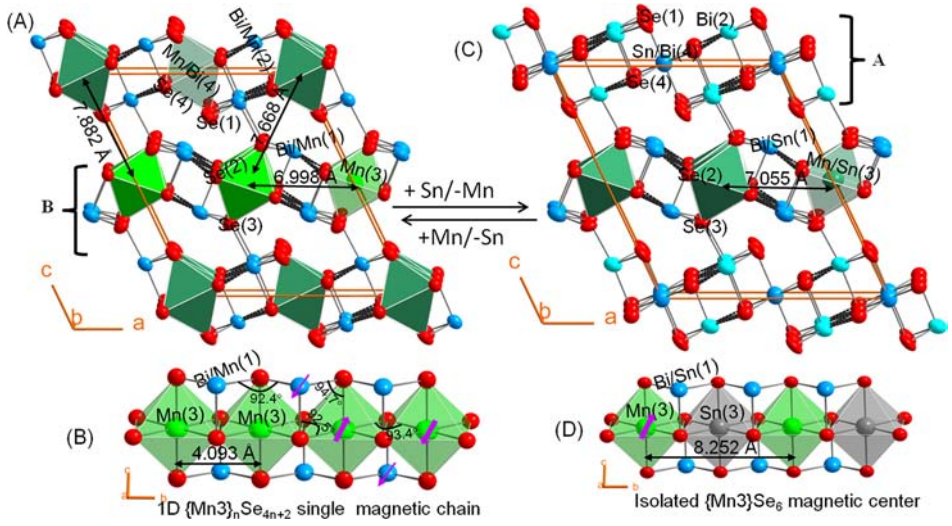

Figure 3. Graphical representation of crystal structure of $Mn_{1-x}Sn_xBi_2Se_4$ ((A) $x = 0$; (C) $x = 0.75$) projected along [010]. (B) Geometrical details of the $\{Mn3\}_nSe_{4n+2}$ single magnetic chain in the structure of $MnBi_2Se_4$; (D) proposed structure of the corresponding $\{M3\}_nSe_{4n+2}$ chain in the structure of $Mn_{0.25}Sn_{0.75}Bi_2Se_4$ assuming a long-range atomic ordering between Mn and Sn within the chain. Ellipsoids correspond to 98% probability level.

were observed on the recorded XPS spectra. The Bi 4d and Bi 4f peaks recorded on $Mn_{1-x}Sn_xBi_2Se_4$ samples are shown in Figure 2, panels C and D, respectively. The binding energy of the Bi $4d_{5/2}$ peak in various $Mn_{1-x}Sn_xBi_2Se_4$ samples range from 441.3 eV ($x = 0$) to 442.2 eV ($x = 0.75$) which are consistent with the value of 441.9 eV reported for Bi $4d_{5/2}$ in Bi_2Se_3.[45] In addition, there is an excellent agreement between the binding energy of the Bi 4f doublet ($4f_{5/2}$: 163.4 eV and $4f_{7/2}$: 158.1 eV) measured in various $Mn_{1-x}Sn_xBi_2Se_4$ samples and the values reported for the corresponding Bi 4f peaks ($4f_{5/2}$: 163.4 eV and $4f_{7/2}$: 158.2 eV) in Bi_2Se_3.[45] Therefore, Bi atoms in the synthesized $Mn_{1-x}Sn_xBi_2Se_4$ samples maintain a 3+ oxidation state. The binding energies of the Se $3d_{5/2}$ peak (Figure S1) recorded on various $Mn_{1-x}Sn_xBi_2Se_4$ samples range between 53.3 eV ($x = 0$) and 55.2 eV ($x = 0.75$), which are within the energy window typically reported for Se^{2-}.[46−48] In summary, it appears from XPS analysis that the substitution of Mn by Sn in $Mn_{1-x}Sn_xBi_2Se_4$ samples is isoelectronic with Mn and Sn adopting the 2+ oxidation state, whereas the valence state of Bi (3+) and Se (2−) remains constant.

Crystal Structure. The investigation of the structures of the Mn-rich ($x = 0$) and the Mn-poor ($x = 0.75$) compositions of the $Mn_{1-x}Sn_xBi_2Se_4$ family of compounds using single crystal X-ray diffraction revealed that the compounds form an

dx.doi.org/10.1021/ja303952w | J. Am. Chem. Soc. 2012, 134, 14033−14042

isomorphic solid-solution series crystallizing in the monoclinic space group $C2/m$ (no.12) and adopting the MSb_2Se_4 (M = Mn, Fe) structure type.[3,4] The refined unit-cell parameters of both compositions (x = 0 and x = 0.75) using X-ray single crystal data showed noticeable increases in all parameters ($\Delta a/a = \Delta b/b$ = 0.8%; $\Delta c/c$ = 0.6%) leading to approximately $\Delta V/V$ = 2.3% expansion of the unit-cell volume (Table 1). This increase in the unit-cell parameters of $Mn_{1-x}Sn_xBi_2Se_4$ with increasing Sn content (increasing x values) is consistent with the large difference (ΔIR/IR = 44%) in the effective ionic radii (IR) of Mn^{2+}(0.83 Å)[40,41] and Sn^{2+}(~1.2 Å) in a 6-fold coordination environment and also confirms the surprisingly high (up to 75%) level of substitution between both elements in the structure of $Mn_{1-x}Sn_xBi_2Se_4$.

The structure of $Mn_{1-x}Sn_xBi_2Se_4$ solid solutions (Figure 3) contains four crystallographically independent metal positions, two general positions M1(4i) and M2(4i) and two special positions M3(2d) and M4(2a) (Table 2). Metal atoms located at the M1 position form a [1 + 2 + 2] distorted square pyramidal geometry of Se atoms with bond distances ranging between 2.717(2) and 3.161(2) Å (Table 3). The M1 position is preferentially occupied by Bi atoms and contains 94%Bi + 6% Mn in the structure of $MnBi_2Se_4$, while 80%Bi + 20%Sn composition was observed in the structure of $Mn_{0.25}Sn_{0.75}Bi_2Se_4$ (Table 2). The M2 position located in a distorted [2 + 1 + 1 + 2] octahedral geometry of Se atoms with bond lengths raging from 2.818(2) to 3.094(2) Å, also showed a strong preference for Bi atoms. In the structure of $MnBi_2Se_4$, the M2 position is mixed occupied by Bi(94%) and Mn(6%), whereas full (100%) Bi occupancy was found in the structure of $Mn_{0.25}Sn_{0.75}Bi_2Se_4$. The M3 position, located in a flattened [2 + 4] octahedral geometry with two short axial bonds (ranging from 2.592(2) to 2.648(2) Å) and four long equatorial bonds (ranging from 2.810(2) to 2.834(2) Å), is preferentially occupied by Mn atoms. In the structure of $MnBi_2Se_4$, the M3 position is fully occupied by Mn atoms, whereas a 50% mixed occupancy between Mn and Sn was observed in the structure of $Mn_{0.25}Sn_{0.75}Bi_2Se_4$. The M4 position, located in a more regular octahedral geometry, with bond lengths between 2.755(2) and 2.863(3) Å, also showed a strong preference for Mn atoms (76%Mn + 24%Bi) in the structure of $MnBi_2Se_4$. In the structure of $Mn_{0.25}Sn_{0.75}Bi_2Se_4$, this atomic position is Mn-free and has a mixed occupancy of 40%Bi + 60%Sn.

By comparing the fraction of Mn atoms at various metal positions within the structures of $MnBi_2Se_4$ (Mn-rich) and $Mn_{0.25}Sn_{0.75}Bi_2Se_4$ (Mn-poor), one can anticipate upon increasing the concentration of Sn in the $Mn_{1-x}Sn_xBi_2Se_4$ solid-solution series, a preferential Mn to Sn substitution within the M1 and M2 positions in the structure of $MnBi_2Se_4$. This Mn to Sn substitution at M1 and M2 position is likely to occur until the fraction of Mn atoms (12%) at both positions in the structure of $MnBi_2Se_4$ is depleted (x = 0.12). For compositions containing more than 12% Sn, the excess Sn atoms is likely to substitute Mn atoms within the M3 and M4 positions with a strong preference for the Mn atoms at the M4 position.

In the crystal structure of $MnBi_2Se_4$, individual $\{M3\}Se_6$ and $\{M4\}Se_6$ octahedra share edges along [010] to form one-dimensional (1D) $\{M3\}_nSe_{4n+2}$ and $\{M4\}_nSe_{4n+2}$ ($1 \le n \le \infty$) single magnetic chains (Figure 3B). Neighboring $\{M4\}_nSe_{4n+2}$ and $\{M3\}_nSe_{4n+2}$ single chains are linked along [100] by weak M2···Se4 (3.019(3) Å) and M1···Se2 (3.130(3) Å) bonds, respectively, to build two kinds of magnetic layers denoted A and B (Figure 2) and alternating along [001]. The shortest distance between nearest neighboring single magnetic chains is 6.998(2) Å within individual layer and 7.668(2) Å between adjacent layers. In the structure of $Mn_{0.25}Sn_{0.75}Bi_2Se_4$, the layer A formed by $\{M4\}_nSe_{4n+2}$ single chains is nonmagnetic due to the full substitution of Mn by Sn at the M4 position (Figure 3C). This drastically increases the interlayer separation between $\{M3\}_nSe_{4n+2}$ single magnetic chains to 15.336(2) Å.

Magnetism. The striking difference in the distribution of magnetic centers (Mn atoms) within the structure of the $Mn_{1-x}Sn_xBi_2Se_4$ solid-solution series upon increasing the concentration of Sn atoms is expected to induce drastic changes in the magnetic behavior of the materials. To probe the variation in the magnetic exchange interactions within the $Mn_{1-x}Sn_xBi_2Se_4$ solid-solutions, magnetic susceptibility measurements on three compositions with x = 0, x = 0.3 and x = 0.75, were performed in the temperature range of 2−300 K using applied fields of 100, 1000, and 10000 Oe. These phases represent three critical regions of the $Mn_{1-x}Sn_xBi_2Se_4$ solid-solution series within which a striking difference in the distribution of Mn atoms in the crystal structure is expected. According to the manganese distribution in the crystal structures of $MnBi_2Se_4$ and $Mn_{0.25}Sn_{0.75}Bi_2Se_4$, one can anticipate the presence of Mn atoms in all four (M1, M2, M3 and M4) atomic positions for compositions with $0 \le x \le 0.12$ (Mn-rich compositions). For compositions with $0.12 \le x \le 0.5$ (intermediate compositions), Mn atoms are expected only within the M3 and M4 positions, while for compositions with $0.5 \le x < 1.0$ (Mn-poor compositions), a strong preferential occupation of the M3 position by Mn atoms is anticipated.

In the structure of $MnBi_2Se_4$ (x = 0), the $\{M4\}_nSe_{4n+2}$ and $\{M3\}_nSe_{4n+2}$ single magnetic chains are 6.998(2) and 7.668(2) Å apart, suggesting weak interchain magnetic exchange interactions. Therefore, the magnetic behavior of the $MnBi_2Se_4$ phase is controlled by the intrachain magnetic exchange interactions. The magnetic susceptibility of $MnBi_2Se_4$ gradually increases with decreasing temperature, reaches a maximum at T_N ~ 15 K, and thereafter continues to decrease with further cooling (Figure 4). The appearance of a broad peak on the susceptibility curves at 15 K suggests antiferromagnetic

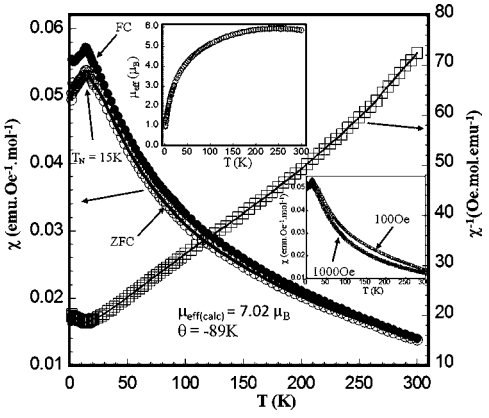

Figure 4. Temperature dependence of the DC magnetic susceptibility (χ) and inverse susceptibility ($1/\chi$) of $MnBi_2Se_4$ measured in an applied magnetic field of 100 Oe. Top inset: Temperature dependence of the effective magnetic moment. Bottom inset: Temperature dependent ZFC susceptibility of $MnBi_2Se_4$ measured at 1000 and 100 Oe .

dx.doi.org/10.1021/ja303952w | J. Am. Chem. Soc. 2012, 134, 14033−14042

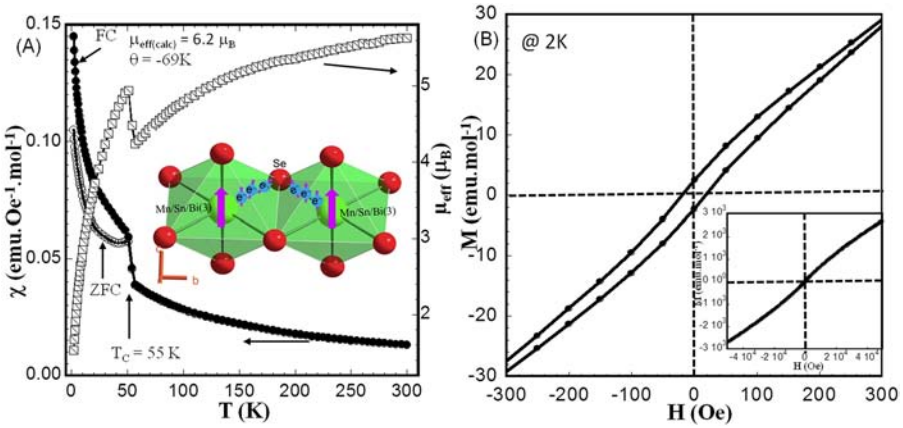

Figure 5. (A) Temperature dependence of the magnetic susceptibility (χ) (measured in an applied magnetic field of 100 Oe under ZFC and FC conditions) and the effective magnetic moment (μ_{eff}) of $Mn_{0.7}Sn_{0.3}Bi_2Se_4$. The inset shows the proposed spin-polarized electron current mediated ferromagnetic coupling between localized magnetic moments on nearest neighboring magnetic centers. (B) Field dependence of the magnetization of $Mn_{0.7}Sn_{0.3}Bi_2Se_4$ measured at 2 K. The inset shows the full graph between −50 and +50 kOe.

exchange interaction between localized spins on nearest neighboring Mn atoms within individual $\{M4\}_nSe_{4n+2}$ and $\{M3\}_nSe_{4n+2}$ single magnetic chains (Figure 3B). This dominant intrachain antiferromagnetic (AFM) exchange interactions is also confirmed by the decrease of the effective magnetic moment (μ_{eff}) from the room temperature value of 5.82 μ_B to ∼1.0 μ_B at 2 K (Figure 4, top-inset). The observed room temperature value of μ_{eff} is very close to the expected theoretical spin only value of 5.92 μ_B for Mn^{2+} ($3d^5$) in the high spin configuration and also confirms our initial assignment of the oxidation state of the Mn ions as +2 from the crystal structure refinement and XPS analysis.

Despite the above strong indicators of predominantly AFM intrachain exchange interactions within the structure of $MnBi_2Se_4$, the divergence of the zero-field-cooled (ZFC) and field-cooled (FC) magnetic susceptibility curves in the whole measured temperature range (2−300 K) and also their dependence on the applied magnetic field (Figure 4, bottom-inset and Figure S2) suggest the existence of residual ferromagnetic (FM) ordering in the sample, which persists up to 300 K. Furthermore, the inverse susceptibility data above the AFM ordering temperature (T_N = 15 K) sharply deviates from the Curie−Weiss law and the fitting of the linear portion of the curve (50−100 K) resulted in a Weiss constant of −89 K and a rather large effective magnetic moment $\mu_{eff(calc)}$ = 7.02 μ_B. This complex magnetic behavior of $MnBi_2Se_4$ (x = 0) can be understood by looking carefully at the geometrical parameters of the single magnetic chains as well as the distribution of Mn atoms between the various metal positions within an individual chain. Within the $\{M4\}_nSe_{4n+2}$ or $\{M3\}_nSe_{4n+2}$ single chains, the electronic configuration of the Mn^{2+} ($3d^5$) center is expected to be $(dxy)^1(dyz)^1(dxz)^1(dz^2)^1(dx^2-y^2)^1$. Therefore, the Mn−Se−Mn bond angle of ∼93.4° points to a mixture of weak ferromagnetic and antiferromagnetic exchange interactions between nearest neighboring Mn atoms according to the Goodenough-Kanamouri rules.[49−51] In addition, the magnetic coupling between neighboring Mn atoms within the chain is also influenced by contributions from localized spins at the M1 or M2 positions (Figure 3B) arising from the partial occupation (6% Mn) of these positions by Mn atoms (Table 2). Depending on the M1−Se−Mn bond angle (92.4° or 94.7°), the residual magnetic moments at M1 or M2 can either align parallel (ferromagnetic coupling) or antiparallel (antiferromagnetic coupling) with respect to the localized moment on the Mn atoms within an individual single chain. These competing FM and AFM exchange interactions between various magnetic centers within individual chains and the magnetic contributions from spins localized at the adjacent M1 and M2 positions are believed to be responsible for the observed divergence of the ZFC and FC susceptibility curves above T_N = 15 K as well as the dependence of the DC magnetic susceptibility on the applied magnetic field. Upon increasing the magnitude of the applied external magnetic field (from 100 Oe to 10 kOe), the divergence between the ZFC and FC magnetic susceptibility curves vanishes when the applied magnetic field reaches 5 kOe and the magnitude of the susceptibility decreases to the minimum values which remain constant with further increase of the applied field to 10 kOe (Figure S2). This suggests that the contribution of the residual magnetic moments at M1 and M2 positions to the overall magnetization of the sample is quenched by the application of the large external magnetic field. This is consistent with the effective magnetic moment, $\mu_{eff(calc)}$ = 5.8 μ_B, calculated using susceptibility data (between 100 and 250 K) recorded under ZFC conditions with an external applied field of 5 kOe.

Upon substituting 30% of the Mn atoms in the structure of $MnBi_2Se_4$ by the nonmagnetic and semimetallic Sn atoms, the resulting phase with composition $Mn_{0.7}Sn_{0.3}Bi_2Se_4$ (calculated from the general formula $Mn_{1-x}Sn_xBi_2Se_4$, x = 0.3) exhibits a strikingly different magnetic behavior. The phase purity of the compound (x = 0.3) was confirmed by combining DSC analysis and X-ray diffraction (XRD) characterization of finely ground polycrystalline powder samples (Figure 1). Furthermore, the excellent match between the experimental XRD pattern of $Mn_{0.7}Sn_{0.3}Bi_2Se_4$ and the theoretical pattern calculated from the single crystal structure refinement of $MnBi_2Se_4$ (Figure 1A) suggests that both phases (x = 0 and x = 0.3) are isostructural. Given, the observed strong preferential occupation of the M3 and M4 atomic positions by Mn atoms from the structure refinement of $MnBi_2Se_4$ (where only ∼12% of the Mn atoms are found at the M1 and M2 positions), we anticipate that at a 30% substitution level between Mn and Sn, all the Mn atoms (12%) originally located within the M1 and M2 positions in the structure of $MnBi_2Se_4$ will be substituted by 12% Sn atoms and the remaining 18%Sn will substitute Mn atoms at both M3 and M4 positions. Therefore, a simple structural model for

dx.doi.org/10.1021/ja303952w | J. Am. Chem. Soc. 2012, 134, 14033−14042

$Mn_{0.7}Sn_{0.3}Bi_2Se_4$ with (94% Bi + 6% Sn) mixed occupancy at both M1 and M2 positions, and (70% Mn + 18% Sn + 12% Bi) mixed occupancy at M3 and M4 positions was refined by Rietveld method using X-ray powder diffraction data. The structure refinement performed using the GSAS[52] package and the EXPGUI interface,[53] yielded satisfactory results (Figure S3, Table S1).

Within this atomic distribution picture, the number of magnetic centers within the structure of $Mn_{0.7}Sn_{0.3}Bi_2Se_4$ is reduced to only the M3 and M4 positions and the accompanying mixture of the magnetic Mn atoms and the semimetallic Sn and Bi atoms at the M3 and M4 positions can lead to a drastic change in the magnetic superexchange interactions between neighboring magnetic centers within individual $\{M4\}_nSe_{4n+2}$ and $\{M3\}_nSe_{4n+2}$ single chains. Indeed, we observed that the effective magnetic moment of $Mn_{0.7}Sn_{0.3}Bi_2Se_4$ at 300 K is μ_{eff} = 5.62 μ_B, which is smaller than the theoretical spin only value of 5.92 μ_B for Mn^{2+} ($3d^5$). This suggests that a significant AFM exchange interaction between neighboring magnetic centers (Mn atoms) within individual magnetic chains is already present at 300 K. Upon cooling, the μ_{eff} value gradually decreases from μ_{eff} = 5.62 μ_B at 300 K to a minimum of 4.2 μ_B at 55 K (Figure 5A). The μ_{eff} value suddenly increases below 55 K reaching a maximum of 4.9 μ_B at 51 K and subsequently decreases sharply to a minimum value of 1.5 μ_B at 2 K with further decreases on temperature. The observed sudden increase of the effective magnetic moment between 55 and 51 K is associated with a strong ferromagnetic coupling between localized spins on adjacent magnetic centers within individual $\{M4\}_nSe_{4n+2}$ and $\{M3\}_nSe_{4n+2}$ single chains. Below 51 K, there is a competition between the ferromagnetic intrachain magnetic coupling and a three-dimensional interchain antiferromagnetic magnetic superexchange interaction leading to a rapid decrease of the μ_{eff} value and large increases in the ZFC and FC magnetic susceptibilities. Above the Curie transition temperature, T_c = 55 K, the magnetic susceptibility of $Mn_{0.7}Sn_{0.3}Bi_2Se_4$ obeys the Curie–Weiss law with a Weiss constant of θ = −69 K and a Curie constant of 4.84 emu·Oe^{1-}·mol^{-1} leading to an effective magnetic moment of $\mu_{eff\ (calc.)}$ = 6.2 μ_B, which is consistent with the expected spin-only value of 5.92 μ_B for Mn^{2+}. To further confirm the low temperature (below 55 K) ferromagnetic character of the $Mn_{0.7}Sn_{0.3}Bi_2Se_4$ phase, isothermal field dependence of the magnetization was performed at 2 K in the 0–50 kOe range. The M versus H plot (Figure 5B) at 2 K showed a magnetic hysteresis with a coercive field, H_c = 26 Oe. However, the saturation of the magnetization was not observed up to an applied field of 50kOe (Figure 5B, inset). The presence of the small hysteresis at 2 K confirms that the $Mn_{0.7}Sn_{0.3}Bi_2Se_4$ phase retains a small ferromagnetic character at low temperatures despite the competing 3D interchain antiferromagnetic interactions.

The exact mechanism of the observed ferromagnetic behavior in the $Mn_{0.7}Sn_{0.3}Bi_2Se_4$ phase is not clear. However, we speculate that the significant difference in the distribution of Mn atoms within the structures of $MnBi_2Se_4$ and $Mn_{0.7}Sn_{0.3}Bi_2Se_4$ is the origin of the striking change in the nature of the magnetic exchange interactions, from antiferromagnetic (for x = 0) to ferromagnetic (for x = 0.30) upon partial substitution between Mn and Sn atoms. A possible rational mechanism of magnetic exchange interactions leading to the surprising ferromagnetic behavior of the $Mn_{0.7}Sn_{0.3}Bi_2Se_4$ can be achieved by taking into account the contributions of free charge carriers resulting from the mixing of Mn/Sn/Bi atoms at the M3 and M4 positions within the crystal structure. The mixing of localized spin-polarized electrons of the Mn atoms and itinerant free electrons of the Sn and Bi atoms within the same atomic positions, is expected to induce a spin-polarized electron current between adjacent magnetic centers within individual $\{M4\}_nSe_{4n+2}$ and $\{M3\}_nSe_{4n+2}$ single chains (Figure 5A, inset). Such a spin-polarized electron current presumably mediates the ferromagnetic coupling between localized magnetic moments on nearest neighboring magnetic centers via a superexchange interaction mechanism through the bridging Se atom. The exact mechanism of the proposed spin-polarized electron current mediated superexchange interaction is still under investigation.

When the fraction of Sn atoms substituting Mn atoms in the structure of $MnBi_2Se_4$ is increased to 75%, the composition of the resulting phase is $Mn_{0.25}Sn_{0.75}Bi_2Se_4$ (calculated from the general formula $Mn_{1-x}Sn_xBi_2Se_4$, x = 0.75). DC magnetic susceptibility measurement on polycrystalline powder of $Mn_{0.25}Sn_{0.75}Bi_2Se_4$ using an applied field of 100 Oe showed featureless ZFC and FC curves where the susceptibility value gradually increases upon cooling from 300 to 2 K (Figure 6).

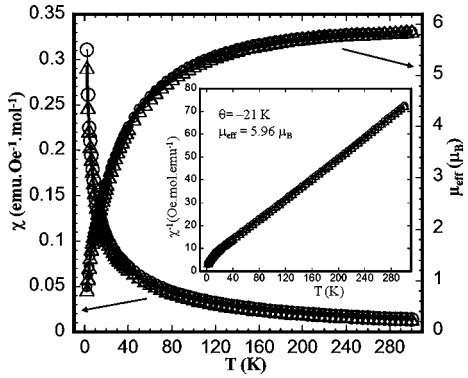

Figure 6. Temperature dependence of the magnetic susceptibility (measured in an applied magnetic field of 100 Oe. FC, circles; ZFC, triangles) and the effective magnetic moment of $Mn_{0.25}Sn_{0.75}Bi_2Se_4$. The inset corresponds to the inverse magnetic susceptibility between 2 and 300 K.

The experimental effective magnetic moment of μ_{eff} = 5.90 μ_B at 300 K is very similar to theoretical value of 5.92 μ_B expected for noninteracting (spin-only) Mn^{2+} ($3d^5$) ions. Upon cooling, the μ_{eff} value decreases to a minimum value of 0.9 μ_B at 2 K. The observed smooth increase in the susceptibility and the similarity between the experimental and theoretical spin-only value of μ_{eff} for Mn^{2+} ions suggests the absence of long-range ordering (LRO) between magnetic centers in the $Mn_{0.25}Sn_{0.75}Bi_2Se_4$ phase. In addition, fitting of the inverse susceptibility data between 2 and 300 K using the Curie–Weiss law yielded an excellent agreement. The small value of the Weiss constant, θ = −21 K, and the effective moment of 5.96 μ_B derived from the fitted data support the absence of exchange interactions between nearest neighboring magnetic centers in $Mn_{0.25}Sn_{0.75}Bi_2Se_4$ (Figure 6, inset). Therefore, $Mn_{0.25}Sn_{0.75}Bi_2Se_4$ can be regarded as a paramagnet over the measured temperature range from 2 to 300 K, although LRO at very low temperatures may still be possible.

The observed magnetic behavior of $Mn_{0.25}Sn_{0.75}Bi_2Se_4$ can be understood through careful examination of structural geometry of the magnetic sublattice. According to our refinement of the

dx.doi.org/10.1021/ja303952w | J. Am. Chem. Soc. 2012, 134, 14033–14042

structure of $Mn_{0.25}Sn_{0.75}Bi_2Se_4$ using single crystal X-ray diffraction, all the 25%Mn atoms in the compound are exclusively located within the M3 position, where a 50% Mn + 50% Sn mixed occupancy was observed. Therefore, the structure of $Mn_{0.25}Sn_{0.75}Bi_2Se_4$ contains only the single magnetic chains $\{M3\}_nSe_{4n+2}$ within which the Mn atoms are diluted with Sn atoms. Given the equal proportion (50%) between Mn and Sn atoms at the M3 position, and the large difference between the ionic radii of Mn^{2+} and Sn^{2+} in 6-fold coordination environment, a local long-range ordering of Mn and Sn within the $\{M3\}_nSe_{4n+2}$ chain leading to a structure with lower energy can be anticipated. One possible model of such long-range ordering consists of alternating Sn and Mn within the $\{M3\}_nSe_{4n+2}$ chain in such a way that one out of two metal positions is fully occupied by Mn atoms (Figure 3D). This should result in a large separation of ~8.252(2) Å between nearest neighboring Mn atoms within the $\{M3\}_nSe_{4n+2}$ single chain and a minimum distance of 7.055(2) Å between Mn atoms from adjacent $\{M3\}_nSe_{4n+2}$ single chains. Within this atomic distribution picture, the resulting large distances between Mn containing sites within the structure inhibit all possible direct and indirect magnetic exchange interactions between nearest neighboring magnetic centers (isolated $\{Mn3\}Se_6$). Therefore, the magnetic behavior of the $Mn_{0.25}Sn_{0.75}Bi_2Se_4$ phase is associated with the interactions of isolated $\{Mn3\}Se_6$ magnetic centers with the applied external magnetic field.

CONCLUDING REMARKS

In summary, we have investigated the crystal structure and magnetic behavior of several compositions of the isomorphic solid-solution series $Mn_{1-x}Sn_xBi_2Se_4$. We found that although gradual Mn to Sn substitution within the $Mn_{1-x}Sn_xBi_2Se_4$ series maintains the crystal structure as essentially unchanged, the magnetic behavior of the resulting material strongly depends on the level of Mn to Sn substitution (x value), which in turn affects the distribution of the remaining Mn atoms throughout the various metal positions in the crystal structure. $MnBi_2Se_4$ (x = 0) is an antiferromagnet with ordering temperature T_N = 15 K. Upon substituting 30% of Mn by Sn atoms, the dominant magnetic exchange coupling within the compound below 51 K is driven from antiferromagnetic for the composition with x = 0 to ferromagnetic. The appearance of the ferromagnetic ordering with T_c = 55 K in the $Mn_{0.7}Sn_{0.3}Bi_2S_{e4}$ composition is attributed to the generation of a spin-polarized electron current between adjacent magnetic centers in individual $\{M4\}_nSe_{4n+2}$ and $\{M3\}_nSe_{4n+2}$ single chains within the structure. The spin-polarized electron current, which originates from the intermixing between localized spin-polarized electrons of the magnetic Mn atoms and itinerant free electrons of the semimetallic Sn and Bi atoms within the same atomic positions, is believed to facilitate the ferromagnetic coupling between neighboring magnetic centers within individual $\{M4\}_nSe_{4n+2}$ and $\{M3\}_nSe_{4n+2}$ single chains via a superexchange mechanism through the bridging Se atom. Increasing the manganese substitution level to 75% Sn results in a purely paramagnetic phase with composition $Mn_{0.25}Sn_{0.75}Bi_2Se_4$. The paramagnetic behavior of this composition is attributed to possible long-range atomic ordering between Mn and Sn within the $\{M3\}_nSe_{4n+2}$ single chain leading to isolated $\{Mn3\}Se_6$ octahedra.

ASSOCIATED CONTENT

Supporting Information

X-ray crystallographic data, in CIF format, for the single crystal structure refinements of $MnBi_2Se_4$ and $Mn_{0.25}Sn_{0.75}Bi_2Se_4$; Figures S1 to S3 and Table S1. This material is available free of charge via the Internet at http://pubs.acs.org.

AUTHOR INFORMATION

Corresponding Author

ppoudeup@umich.edu

Notes

The authors declare no competing financial interest.

ACKNOWLEDGMENTS

This work was supported by the National Science Foundation (Career Award DMR-1237550).

REFERENCES

(1) Poudeu, P. F. P.; Takas, N.; Anglin, C.; Eastwood, J.; Rivera, A. *J. Am. Chem. Soc.* **2010**, *132*, 5751.
(2) Poudeu, P. F. P.; Djieutedjeu, H.; provisionary U.S. patent application 61/385206; University of New Orleans: Louisiana, USA, 2011.
(3) Djieutedjeu, H.; Poudeu, P. F. P.; Takas, N. J.; Makongo, J. P. A.; Rotaru, A.; Ranmohotti, K. G. S.; Anglin, C. J.; Spinu, L.; Wiley, J. B. *Angew. Chem., Int. Ed.* **2010**, *49*, 9977.
(4) Djieutedjeu, H.; Makongo, J. P. A.; Rotaru, A.; Palasyuk, A.; Takas, N. J.; Zhou, X. Y.; Ranmohotti, K. G. S.; Spinu, L.; Uher, C.; Poudeu, P. F. P. *Eur. J. Inorg. Chem.* **2011**, 3969.
(5) Anglin, C.; Takas, N.; Callejas, J.; Poudeu, P. F. P. *J. Solid State Chem.* **2010**, *183*, 1529.
(6) Wu, T.; Khazhakyan, R.; Wang, L.; Bu, X. H.; Zheng, S. T.; Chau, V.; Feng, P. Y. *Angew. Chem., Int. Ed.* **2011**, *50*, 2536.
(7) Gao, J. H.; Gu, H. W.; Xu, B. *Acc. Chem. Res.* **2009**, *42*, 1097.
(8) Rao, M. L.; Shamsuzzoha, M.; Gupta, A. *J. Cryst. Growth* **2007**, *306*, 321.
(9) Tsamourtzi, K.; Song, J. H.; Bakas, T.; Freeman, A. J.; Trikalitis, P. N.; Kanatzidis, M. G. *Inorg. Chem.* **2008**, *47*, 11920.
(10) Bu, X. H.; Zheng, N. F.; Feng, P. Y. *Chem.—Eur. J.* **2004**, *10*, 3356.
(11) Wu, M.; Emge, T. J.; Huang, X. Y.; Li, J.; Zhang, Y. *J. Solid State Chem.* **2008**, *181*, 415.
(12) Makovicky, E. *Rev. Mineral. Geochem.* **2006**, *61*, 7.
(13) Makovicky, E. *Eur. J. Mineral.* **1993**, *5*, 545.
(14) Kanatzidis, M. G. *Acc. Chem. Res.* **2005**, *38*, 359.
(15) Eichhorn, B. W. *Prog. Inorg. Chem.* **1994**, *42*, 139.
(16) Kanatzidis, M. G.; Sutorik, A. C. *Prog. Inorg. Chem.* **1995**, *43*, 151.
(17) Mrotzek, A.; Kanatzidis, M. G. *Acc. Chem. Res.* **2003**, *36*, 111.
(18) Chung, D. Y.; Hogan, T.; Brazis, P.; Rocci-Lane, M.; Kannewurf, C.; Bastea, M.; Uher, C.; Kanatzidis, M. G. *Science* **2000**, *287*, 1024.
(19) Kanatzidis, M. G. *Semicond. Semimetals* **2001**, *69*, 51.
(20) Dagenais, M.; Auston, D. H.; Ballman, A. A.; Bhattacharya, P.; Bjorklund, G. J.; Bowden, C.; Boyd, R. W.; Brody, P. S.; Burnham, R.; Byer, R. L.; Carter, G.; Chemla, D.; Dohler, G.; Efron, U.; Eimerl, D.; Feigelson, R. S.; Feinberg, J.; Feldman, B. J.; Garito, A. F.; Garmire, E. M.; Gibbs, H. M.; Glass, A. M.; Goldberg, L. S.; Gunshor, R. L.; Gustafson, T. K.; Hellwarth, R. W.; Kaplan, A. E.; Kelley, P. L.; Leonberger, F. J.; Lytel, R. S.; Majerfeld, A.; Menyuk, N.; Meredith, G. R.; Neurgaonkar, R. R.; Peyghambarian, N. G.; Prasad, P.; Rakuljic, G.; Shen, Y. R.; Smith, P. W.; Stamatoff, J.; Stegeman, G. I.; Stillman, G.; Tang, C. L.; Temkin, H.; Thakur, M.; Valley, G. C.; Wolff, P. A.; Woods, C. *Appl. Opt.* **1987**, *26*, 211.
(21) Liao, J. H.; Marking, G. M.; Hsu, K. F.; Matsushita, Y.; Ewbank, M. D.; Borwick, R.; Cunningham, P.; Rosker, M. J.; Kanatzidis, M. G. *J. Am. Chem. Soc.* **2003**, *125*, 9484.

(22) Zhang, Q. C.; Liu, Y.; Bu, X. H.; Wu, T.; Feng, P. Y. *Angew. Chem., Int. Ed.* **2008**, *47*, 113.
(23) Kanno, R.; Hata, T.; Kawamoto, Y.; Irie, M. *Solid State Ionics* **2000**, *130*, 97.
(24) Matsushita, Y.; Kanatzidis, M. G. *Z. Naturforsch., B* **1998**, *53*, 23.
(25) Ruck, M.; Poudeu, P. F. P. *Z. Anorg. Allg. Chem.* **2008**, *634*, 482.
(26) Ruck, M.; Poudeu, P. F. P. *Z. Anorg. Allg. Chem.* **2008**, *634*, 475.
(27) Ruck, M.; Poudeu, P. F. P.; Sohnel, T. *Z. Anorg. Allg. Chem.* **2004**, *630*, 63.
(28) Poudeu, P. F. P.; Sohnel, T.; Ruck, M. *Z. Anorg. Allg. Chem.* **2004**, *630*, 1276.
(29) Poudeu, P. F. P.; Kanatzidis, M. G. *Chem. Commun.* **2005**, 2672.
(30) Poudeu, P. F. P.; Ruck, M. *Acta Crystallogr., C* **2005**, *61*, I41.
(31) Skowron, A.; Brown, I. D. *Acta Crystallogr.* **1990**, *C46*, 2287.
(32) Makovicky, E.; Mumme, W. G.; Watts, J. A. *Can. Mineral.* **1977**, *15*, 339.
(33) Lee, S.; Fischer, E.; Czerniak, J.; Nagasundaram, N. *J. Alloys Compd.* **1993**, *197*, 1.
(34) Kurowski, D. Ph.D. Thesis, University of Regensburg, Germany, 2003.
(35) Sheldrick, G. M.; Bruker Analytical X-ray Instruments, Inc., Madison, WI., 2000.
(36) Brese, N. E.; Okeeffe, M. *Acta Crystallogr., Sect. B: Struct. Sci.* **1991**, *47*, 192.
(37) Brandenburg, K.; Crystal Impact GbR, Bonn, Germany: 2005.
(38) Vicente, C. P.; Tirado, J. L.; Adouby, K.; Jumas, J. C.; Toure, A. A.; Kra, G. *Inorg. Chem.* **1999**, *38*, 2131.
(39) Goldschmidt, V. M. *J. Chem. Soc.* **1937**, 655.
(40) Shannon, R. D. *Acta Crystallogr., Sect. A* **1976**, *32*, 751.
(41) Shannon, R. D.; Prewitt, C. T. *Acta Crystallogr., Sect. B: Struct. Crystallogr. Cryst. Chem.* **1969**, *B 25*, 925.
(42) Franzen, H.; Sterner, C. *J. Solid State Chem.* **1978**, *25*, 227.
(43) Zhang, W. X.; Yang, Z. H.; Liu, J. W.; Zhang, L.; Hui, Z. H.; Yu, W. C.; Qian, Y. T.; Chen, L.; Liu, X. M. *J. Cryst. Growth* **2000**, *217*, 157.
(44) Ettema, A. R. H. F.; Degroot, R. A.; Haas, C.; Turner, T. S. *Phys. Rev. B* **1992**, *46*, 7363.
(45) Ismailm, F. M.; Hanafi, Z. M. *Z. Phys. Chem. (Leipzig)* **1986**, *267*, 667.
(46) Shalvoy, R. B.; Fisher, G. B.; Stiles, P. J. *Phys. Rev. B* **1977**, *15*, 1680.
(47) Mandale, A. B.; Badrinarayanan, S.; Date, S. K.; Sinha, A. P. B. *J. Electron Spectrosc.* **1984**, *33*, 61.
(48) Ueno, T. *Jpn. J. Appl. Phys.* **1983**, *22*, 1349.
(49) Goodenough, J. B. *Phys. Rev.* **1955**, *100*, 564.
(50) Goodenough, J. B. *J. Phys. Chem. Solids* **1958**, *6*, 287.
(51) Kanamori, J. *J. Phys. Chem. Solids* **1959**, *10*, 87.
(52) Larson, A. C.; Von Dreele, R. B. *General Structure Analysis System (GSAS)*; Report LAUR 86-748; Los Alamos National Laboratory: Los Alamos, NM, 2000.
(53) Toby, B. H. *J. Appl. Crystallogr.* **2001**, *34*, 210.